RESEARCH ARTICLE

Line-field confocal optical coherence tomography as a tool for three-dimensional in vivo quantification of healthy epidermis: A pilot study

Julie Chauvel-Picard[1] | Vincent Bérot[2] | Linda Tognetti[3] |
Carmen Orte Cano[4] | Margot Fontaine[4] | Clément Lenoir[4] |
Javiera Pérez-Anker[5,6] | Susana Puig[5,6] | Arnaud Dubois[7] | Sandra Forestier[8] |
Jilliana Monnier[9,10] | Randa Jdid[8] | Gabriel Cazorla[8] |
Mélanie Pedrazzani[11] ⓘ | Antoine Sanchez[11,12] | Sébastien Fischman[11] |
Pietro Rubegni[3] | Véronique del Marmol[4] | Joseph Malvehy[5,6] |
Elisa Cinotti[3,10] ⓘ | Jean L. Perrot[2,10] | Mariano Suppa[4,10,13]* ⓘ

[1]Department of Craniomaxillofacial Surgery, University Hospital of Saint-Etienne, Saint-Etienne, France

[2]Department of Dermatology, University Hospital of Saint-Etienne, Saint-Etienne, France

[3]Dermatology Unit, Department of Medical, Surgical and Neurological Sciences, University of Siena, Siena, Italy

[4]Department of Dermatology, Hôpital Erasme, Université Libre de Bruxelles, Brussels, Belgium

[5]Melanoma Unit, Hospital Clinic Barcelona, University of Barcelona, Barcelona, Spain

[6]CIBER de enfermedades raras, Instituto de Salud Carlos III, Barcelona, Spain
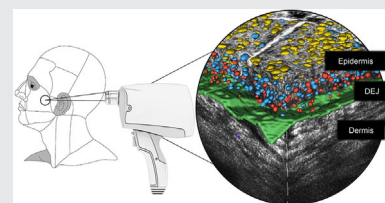
[7]Université Paris-Saclay, Institut d'Optique Graduate School, Laboratoire Charles Fabry, Palaiseau, France

[8]Chanel Parfums Beauté, Innovation Research and Development, Pantin, France

[9]Department of Dermatology and Skin Cancer, la Timone hospital, Assistance Publique-Hôpitaux de Marseille, Aix-Marseille University, Marseille, France

Abstract

Epidermal three-dimensional (3D) topography/quantification has not been completely characterized yet. The recently developed line-field confocal optical coherence tomog-

raphy (LC-OCT) provides real-time, high-resolution, in-vivo 3D imaging of the skin. This pilot study aimed at quantifying epidermal metrics (epidermal thicknesses, dermal-epidermal junction [DEJ] undulation and keratinocyte number/shape/size) using 3D LC-OCT. For each study participant (8 female, skin-type-II, younger/older volunteers), seven body sites were imaged with LC-OCT. Epidermal metrics were calculated by segmentations and measurements assisted by artificial intelligence (AI) when appropriate. Thicknesses of epidermis/SC, DEJ undulation and keratinocyte nuclei volume varied across body sites. Evidence of keratinocyte maturation was observed in vivo: keratinocyte nuclei being small/spherical near the DEJ and flatter/elliptical near the skin surface. Skin microanatomy can be quantified by combining LC-OCT and AI. This technology could be highly relevant to understand aging processes and conditions linked to epidermal disorders. Future clinical/research applications are to be expected in this scenario.

Julie Chauvel-Picard and Vincent Bérot should be considered joint first author.

Elisa Cinotti, Jean-Luc Perrot and Mariano Suppa should be considered joint senior author.

[10]Groupe d'Imagerie Cutanée Non Invasive (GICNI) of the Société Française de Dermatologie (SFD), Paris, France

[11]DAMAE Medical, Paris, France

[12]Department of Bioengineering, South Kensington Campus, Imperial College London, London, UK

[13]Institut Jules Bordet, Université Libre de Bruxelles, Brussels, Belgium

*Correspondence
Prof Mariano Suppa, Department of Dermatology, Hôpital Erasme, Université Libre de Bruxelles, Route de Lennik 808, 1070 Brussels, Belgium.
Email: dr.marianosuppa@gmail.com

1 | INTRODUCTION

The recent advent of reflectance confocal microscopy (RCM) and optical coherence tomography (OCT) have made it possible to study cellular features within the skin, in real time and in vivo. Although OCT has successfully illustrated the variety of epidermal thicknesses between body sites [1], it has limited lateral and axial resolution, making it difficult to segment individual epidermal cells using this technology. Conversely, RCM can successfully visualize healthy skin features such as epidermal pigmentation, keratinocytes and collagen network [2–5], and quantify the density of dermal papillae with high lateral resolution [6]. However, having a non-isotropic spatial resolution (axial resolution lower than lateral one), RCM appears non-ideal in describing the three-dimensional (3D) morphology of the dermal-epidermal junction (DEJ) and keratinocyte network.

Line-field confocal optical coherence tomography (LC-OCT) is a new, non-invasive imaging technique that produces in vivo 3D images of cutaneous cellular architecture with a quasi-isotropic resolution close to 1 μm down to a depth of 500 μm [7–10]. LC-OCT produces vertical and horizontal sectional images with near-histological resolution in real time. Image stacks can also be acquired to build 3D images. These 3D images enable the epidermal thickness to be measured and cell numbers, layers and size quantified.

Accurate, quantified cartography of the epidermis—including the DEJ—are important for clinical research, diagnostics and skin disease management [11, 12]. Although current non-invasive skin imaging techniques have provided some qualitative and quantitative data about skin morphology, little is known about the 3D topographical characteristics of the epidermis and the quantification of cellular structures in vivo.

The objective of this pilot study was to provide an in vivo, quantitative analysis of healthy epidermis by means of a 3D LC-OCT device: to this scope, we aimed at quantifying in three dimensions the thickness of the epidermis, the undulation of the DEJ, and the keratinocyte number, shape and size using artificial intelligence (AI).

2 | MATERIALS AND METHODS

2.1 | Study population

This pilot study involved female volunteers aged between 20–30 (younger group) and 50–60 years (older group) with Fitzpatrick's phototype II skin. Gender and phototype were restricted as such to ensure a homogeneous sample and to reduce the risk of inter-individual variability. The study was performed at *Chanel Parfums Beauté* research center, Pantin, Greater Paris, France, during 3 days in February 2020. Participants were excluded if they were allergic to paraffin oil needed to acquire LC-OCT images.

The research was conducted according to the principles expressed in the Declaration of Helsinki, and written informed consent was obtained from all participants.

For each study participant, seven body sites were explored: three on the head (central forehead, tip of the nose, right cheek), two on the trunk (pre-sternal chest and mid-back), two on the upper limbs (mid-dorsal side of the right forearm, mid-dorsal side of the right hand).

2.2 | LC-OCT device

In this study, we used a LC-OCT device (DAMAE Medical, Paris) which painlessly and non-invasively produces vertically-oriented (histology-like) and horizontally-oriented (RCM-like) sectional images as well as full 3D volume block images.

The device uses a two-beam interference microscope with supercontinuum laser at a central wavelength of 800 nm and a line-scan camera as a detector. The light emitted from the device and entering the skin is safe (class 1 according to EN 60825-1). LC-OCT measures the time of flight and amplitude of light backscattered from the tissue microstructures illuminated by a line-shaped light. This technology combines the OCT interferometry principle with the confocal spatial filtering of RCM. The LC-OCT device has three imaging modalities: vertical or *en coupe* (similar to conventional OCT), horizontal or *en face* (comparable with RCM) and 3D stacks. The vertical and horizontal sectional images are produced in real time at eight frames per second. The images can be acquired up to a depth of about 500 μm. They have an axial resolution of 1.1 μm, a lateral resolution of 1.3 μm and a field of view of 1.2 mm × 0.4 mm (vertical) and 1.2 mm × 0.5 mm (horizontal). Complete technical details are described elsewhere [7, 9, 13].

2.3 | Image acquisition

A single operator (RJ) acquired the LC-OCT images. The probe was applied to a healthy skin area clinically void of moles or pigmented spots. A glass window at the end of the LC-OCT probe provides a mechanical interface between the probe and the skin that stabilizes the imaging area. Dermoscopic oil applied to the skin surface provided refractive index matching. The images were visualized in real time and 3D volumes were saved for quantitative measurement. 3D LC-OCT blocks were recorded as stacks of slices (1.2×0.5 mm^2) parallel to the skin surface with a 1 μm step size up to a depth of 500 μm (total block volume $1.2 \times 0.5 \times 0.5$ mm^3). This procedure was repeated for each body site, as previously executed in a similar 2D LC-OCT study performed by our group [14]. A stable position of the device on the skin is required during the 3D acquisition that typically lasts about 20 seconds to reach the total depth of the epidermis. Image acquisition may have been compromised on some body areas, such as breathing movement on the pre-sternal chest. However, acquisitions without motion artifacts were analyzed, thus reducing the risk of measurements being affected by the acquisition conditions.

2.4 | Segmentation and measurements

2.4.1 | SC thickness

For each participant, five evenly distributed vertical images were automatically extracted from the 3D stack.

On each image, a semi-automated segmentation of both the skin surface and the junction between the SC and the stratum granulosum (SG) was then performed. This process was supervised by a trained operator (MP) and additional control nodes, forcing the segmentations to adjust, were added to improve the precision if needed. The SC thickness was defined as the average distance between the skin surface and the junction between SC and SG.

2.4.2 | Epidermal thickness

A full 3D analysis was performed to compute the epidermal thickness due to the highly undulated DEJ. A dedicated fast marching algorithm was performed to segment the skin surface and the DEJ. The segmentation result was reviewed by a trained operator (MP) and additional control nodes were added to fine tune the segmentation. The epidermal thickness was defined as the average distance between the top of the SC and the DEJ. We also measured the epidermal thickness deprived of the SC, that is, the SG and stratum spinosum (SS), expressed in μm ± standard deviation (SD). Hair follicles were excluded from this analysis.

2.4.3 | DEJ undulation

The above-mentioned semi-automated segmentation technique was employed. The amplitude of the DEJ undulations was determined within the region of interest (ROI) area (horizontal plane). The interdigitation index [15] was calculated using the following formula and expressed in percentage (%) ± SD: $I = \frac{S_{DEJ}}{S_{ROI}} - 1$, with S_{DEJ} being the area of the DEJ layer and S_{ROI} being the area of the ROI.

2.4.4 | Keratinocyte nuclei

Keratinocytes were segmented using a deep learning model (AI algorithm) based on 3D convolutions. To train this model, 3D ground truth stacks were pixel-wise labeled using a semi-automated procedure based on morphological criteria and an expert operator (AS) manually removed or added missing nuclei. For this study, a total of 30 3D stacks, measuring $340 \times 560 \times 90$ μm were labeled. These stacks were obtained from a different, ongoing investigation on female volunteers (unpublished data). The stacks were chosen based on image quality (i.e., nuclei visibility in the epidermis) and were consecutively included in the training set. Training was performed on 25 3D stacks while the remaining 5 stacks were used for validation and early stopping. Standard data augmentation techniques [16] were used to increase the dataset size. The model was

trained on patches measuring $60 \times 128 \times 128$ pixels. Random cropping and 3D augmentations (noise and flipping) made it possible to create numerous different training patches (200 epochs of 100 augmented patches per epoch emulating 20 000 different training patches).

The architecture used was 3D StarDist model [17] since it detects 3D star-convex shapes at instance level, similar to keratinocyte nuclei. This deep learning model, based on a variant of a 3D ResNet18, was trained from scratch without transfer learning as no known pretrained weights were available for a similar task up to now. StarDist3D uses 3D convolutions to predict at voxel level (3D pixel) the probability of being the center of a nucleus and the length of the different radii defining the nucleus. We used 96 radii, defined from a 3D Fibonacci lattice, to accurately account for 3D nuclei diversity. The probability threshold for cell detection and the Non-Maximum Suppression threshold were set to 0.5 and 0.05, respectively, allowing touching but non-overlapping cells to be detected.

The precision of the AI algorithm used here was not quantitatively evaluated as the ground truth labels used for training the deep learning model contained some noise. This made computing reliable quantitative measurements of model performances very difficult. Therefore, an expert operator (MP) performed a qualitative review of all images and segmentations included in this study to ensure that all LC-OCT and segmented nuclei were superposable. After this qualitative control, quantitative measurements of nuclei density, volume, compactness and number of cell layers were then performed from the segmented nuclei 3D stacks.

Cell density was described as the quotient of the total number of nuclei in the epidermis by skin surface area and expressed as cell number/mm^2 (rather than in cell number/mm^3 as cell density is heterogeneous throughout the epidermal thickness).

Nucleus volume was computed using the detected polyhedra and expressed in µm^3. For each 3D stack, the nuclei were sorted by their volume and separated into five categories, from the smallest (quintile I) to the largest (quintile V), each quintile containing 20% of the total number of nuclei. For each quintile, we reported the average nuclei volume ± SD.

Compactness is a measure of nucleus sphericity which was calculated from the 3D surface area of the nucleus (A) and cell volume (V) ($36\Pi V^2/A^3$). The compactness score ranged from 0 to 1, where 1 represents a perfect sphere. This measurement was first proposed by Wadell et al. [18] and was later used to describe tumor shapes [19] and characterize red blood cell surface area and deformity [20]. For each 3D stack, the nuclei were sorted by their compactness and separated into five categories, from the least compact (quintile I) to the most compact (quintile V), each quintile containing 20% of the total number of nuclei. For each quintile, we reported the average nuclei compactness ± SD.

The number of cell layers was calculated from the average number of cells crossed on the vertical axis between the SC/SG junction and the DEJ, expressed in average ± SD.

2.5 | Statistical analysis

Continuous variables are presented as mean with SD. Considering the small sample size, the influence of age and body sites was investigated using Mann-Whitney-Wilcoxon test. Pairwise correlation between the different metrics was analyzed based on Spearman's rank correlation coefficients. All tests were two-tailed and considered significant for P-values <.05. The analysis was carried out using R version 4.0.0 (R Foundation for Statistical Computing; Vienna, Austria).

3 | RESULTS

A total of 8 women were included, 5 aged between 20 and 30 (mean age 24.2 ± 2.4 years) and 3 aged between 50 and 60 (mean age 57.0 ± 1.0 year). Seven body sites were imaged for each participant, thus creating a total of 56 LC-OCT image blocks, corresponding to 28 000 vertical images.

The thickness of the SC, SS, the whole epidermis and the DEJ undulation index differed among the 7 body sites (Table 1, Figure 1). The SC was significantly thicker on the mid-dorsal hand than all other body sites. The highest SC thickness was detected on the mid-dorsal hand (24.1 ± 4.6 µm) and the lowest on the cheek (10.0 ± 1.3 µm): these two figures were significantly different ($P < .001$). The SS thickness was significantly higher on the forehead, nose and dorsal hand (average 70.8 ± 11.6 µm) than on cheek, chest, back and dorsal forearm (46.7 ± 6.6 µm, $P < .001$, data not shown). The highest epidermal thickness was found on the dorsal hand (92.9 ± 11.3 µm) and the lowest on the chest (53.7 ± 6.5 µm): these values were significantly different ($P < .001$).

The DEJ undulation varied between volunteers and body sites. The cheek revealed the flattest DEJ ($7.3 \pm 1.3\%$), which was significantly flatter than all the other body sites combined ($18.5 \pm 9.8\%$, $P < .001$, data not shown). Furthermore, the DEJ undulation index was significantly different across facial regions, being flatter on the cheek ($7.3 \pm 1.3\%$) and more undulated on the forehead ($20.8 \pm 10.5\%$). No significant differences were observed between the two age groups.

Similarly, keratinocyte density and number of cell layers varied across body sites. The chest (cell density 35 555 $\pm$ 4715 mm^{-2}; cell layers 4.1 ± 0.5) was

TABLE 1 Epidermal and dermal-epidermal junction quantifications resulting from the segmentation of the skin layers

Body site	SC thickness (µm)		SS thickness (µm)		Epidermis thickness (µm)		DEJ undulation (%)	
Forehead	11.7 (2.1)	11.6 (2.5)	69.5 (13.5)	69.4 (11.8)	81.2 (13.4)	81.0 (12.7)	20.8 (10.5)	22.2 (9.6)
		11.8 (1.8)		69.7 (19.0)		81.5 (17.3)		18.6 (13.9)
Nose	12.6 (2.8)	13.0 (3.4)	**74.3 (13.5)**	76.4 (9.6)	86.9 (12.1)	89.5 (7.0)	18.7 (9.0)	20.7 (11.0)
		11.9 (1.6)		70.6 (20.5)		82.5 (19.1)		15.4 (3.5)
Cheek	10.0 (1.3)	9.7 (1.6)	47.6 (4.6)	49.7 (4.2)	57.6 (4.5)	59.4 (4.6)	7.3 (1.3)	7.0 (1.5)
		10.6 (0.6)		44.1 (3.2)		54.6 (2.8)		7.7 (0.8)
Chest	11.6 (2.0)	12.1 (1.9)	42.1 (6.2)	43.6 (7.6)	53.7 (6.5)	55.7 (7.4)	16.9 (6.8)	18.3 (7.8)
		10.7 (2.0)		39.6 (2.3)		50.3 (3.2)		14.5 (5.3)
Back	12.3 (2.1)	11.5 (1.7)	48.4 (7.0)	48.6 (7.8)	60.8 (7.0)	60.1 (6.7)	**29.6 (10.4)**	26.1 (9.4)
		13.7 (2.2)		48.2 (6.9)		61.9 (8.9)		35.4 (11.0)
Dorsal forearm	15.2 (3.9)	14.9 (3.2)	48.9 (7.0)	49.4 (4.4)	64.0 (6.6)	64.3 (5.1)	14.2 (6.0)	14.6 (7.6)
		15.6 (5.6)		48.0 (11.4)		63.6 (10.0)		13.5 (2.9)
Dorsal part of hand	**24.1 (4.6)**	22.3 (1.0)	68.7 (7.6)	66.3 (5.7)	**92.9 (11.3)**	88.7 (5.9)	11.1 (4.9)	10.2 (5.9)
		27.1 (7.0)		72.7 (10.0)		99.8 (16.2)		12.6 (3.4)

Note: The results are expressed as mean (SD). For each metric, the first column shows the overall mean value and the second column the mean value for the younger group (top line) and older group (bottom line). The largest value for each metric is shown in bold type.

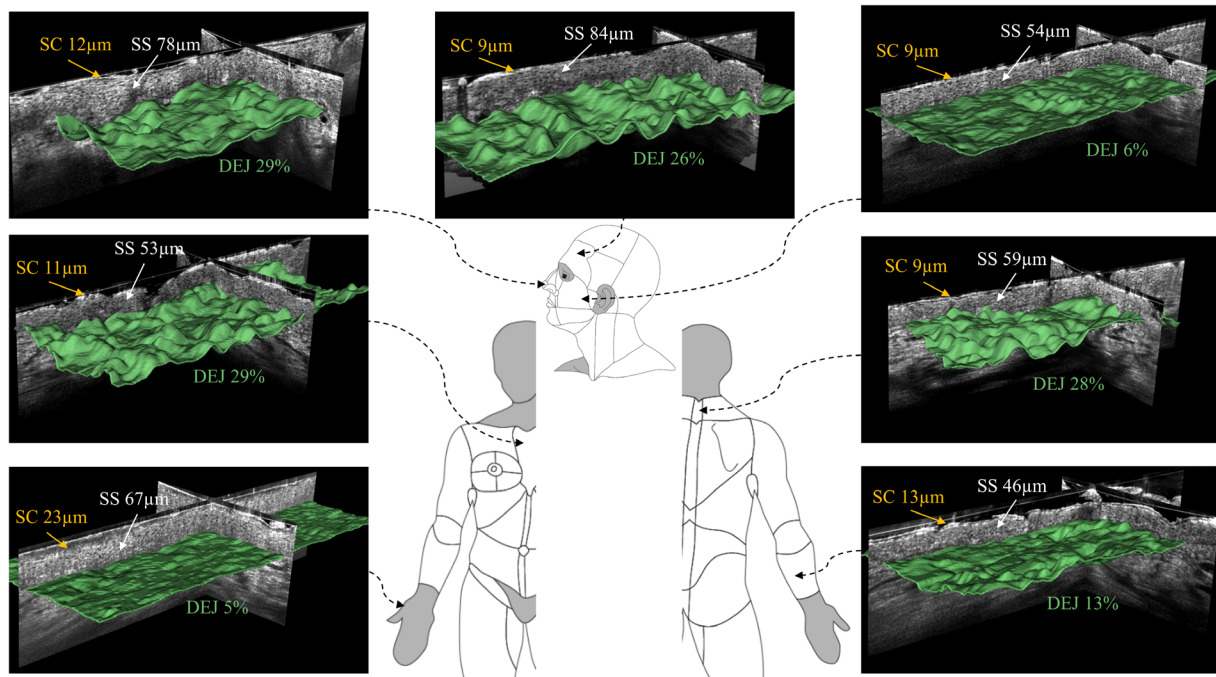Abbreviations: DEJ, dermal-epidermal junction; SC, stratum corneum; SS, stratum spinosum.

FIGURE 1 3D LC-OCT quantification of epidermal characteristics in seven body sites on the same subject (27-year-old female, phototype II). The thickness of stratum corneum (SC) and stratum spinosum (SS) are reported in µm, whereas the undulation of the dermal-epidermal junction (DEJ, green layer) is expressed in percentage

significantly different from the nose (cell density 57 120 ± 6852 mm^{-2}; cell layers 7.4 ± 0.8; P = .002; Table 2). No differences were observed between younger and older skin. Number of cell layers was highly correlated with both keratinocyte density (r^2 = 0.94, $P < .001$; Figure 2A) and SS thickness (r^2 = 0.96, $P < .001$; Figure 2B).

Table 3 illustrates the variation of keratinocytes nuclei volume and compactness across different body sites and age groups.

The largest keratinocyte nuclei (quintile V) had a mean volume of $353 \pm 40 \ \mu m^3$, which was significantly higher than the mean volume of the smallest nuclei (quintile I, $72 \pm 3 \ \mu m^3$, $P < .001$). The volume of the keratinocyte nuclei differed across body sites and age groups. Significantly larger nuclei were observed on the nose ($403 \pm 21 \ \mu m^3$) compared to the back ($311 \pm 18 \ \mu m^3$, $P = .005$). Keratinocyte nuclei were larger in older participants than in younger ones on all body sites except the chest. The biggest difference was observed on the cheek ($396 \pm 36 \ \mu m^3$ in older vs $329 \pm 18 \ \mu m^3$ in younger participants, $P = .05$).

The most compact (rounded) keratinocyte nuclei (quintile V) had 0.85 ± 0.01 compactness which was significantly higher than the compactness of the least compact (flattest) nuclei (quintile I, 0.60 ± 0.03, $P < .001$). The keratinocyte compactness did not differ across body sites and age groups.

TABLE 2 Keratinocyte density and number of cell layers in the skin samples from various body sites

Body site	Keratinocyte density (mm^{-2})		Number of cell layers	
Forehead	56 364 (9678)	57 713 (7100)	6.9 (1.3)	7.0 (1.1)
		54 115 (14 659)		6.7 (1.9)
Nose	**57 120 (6852)**	55 575 (7973)	**7.4 (0.8)**	7.2 (0.9)
		60 209 (3925)		7.9 (0.1)
Cheek	40 239 (5741)	42 823 (3021)	4.7 (0.5)	4.9 (0.4)
		35 932 (7252)		4.4 (0.5)
Chest	35 555 (4715)	36 421 (7063)	4.1 (0.5)	4.1 (0.7)
		34 688 (1855)		4.0 (0.2)
Back	44 274 (6903)	47 574 (7148)	5.1 (0.8)	5.5 (0.7)
		39 324 (2598)		4.5 (0.5)
Dorsal forearm	39 966 (3733)	41 719 (2549)	4.8 (0.5)	4.8 (0.1)
		37 336 (4437)		4.9 (1.1)
Dorsal part of hand	54 009 (4092)	53 216 (1975)	6.4 (0.7)	6.2 (0.4)
		55 331 (6827)		6.8 (0.9)
Global	47 438 (10 255)	48 864 (8884)	5.7 (1.4)	5.8 (1.2)
		45 219 (12 019)		5.6 (1.6)

Note: The results are expressed as mean (SD). For each metric, the first column shows the overall mean value and the second column the mean value for the younger group (top line) and older group (bottom line). The largest value for each metric is shown in bold type.
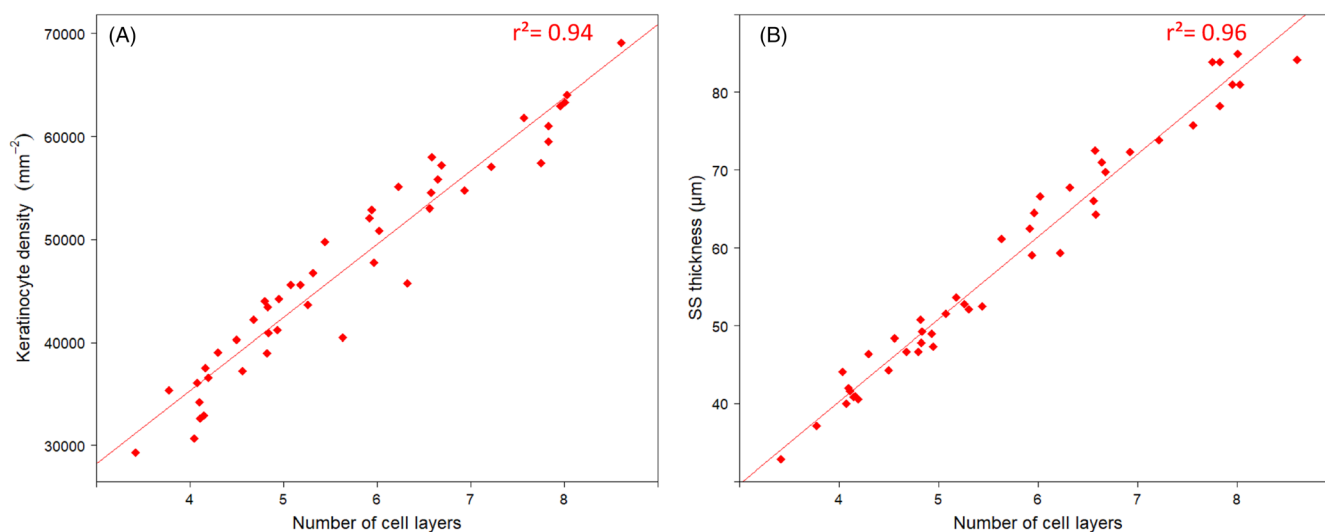

FIGURE 2 Correlation between thickness, keratinocyte density and number of cell layers in stratum spinosum. A, A direct, linear correlation was detected between keratinocyte density and number of cell layers in the stratum spinosum (SS) ($r^2 = 0.94$, $P < .001$). B, A direct, linear correlation was detected between thickness and number of cell layers in the stratum spinosum (SS) ($r^2 = 0.96$, $P < .001$)
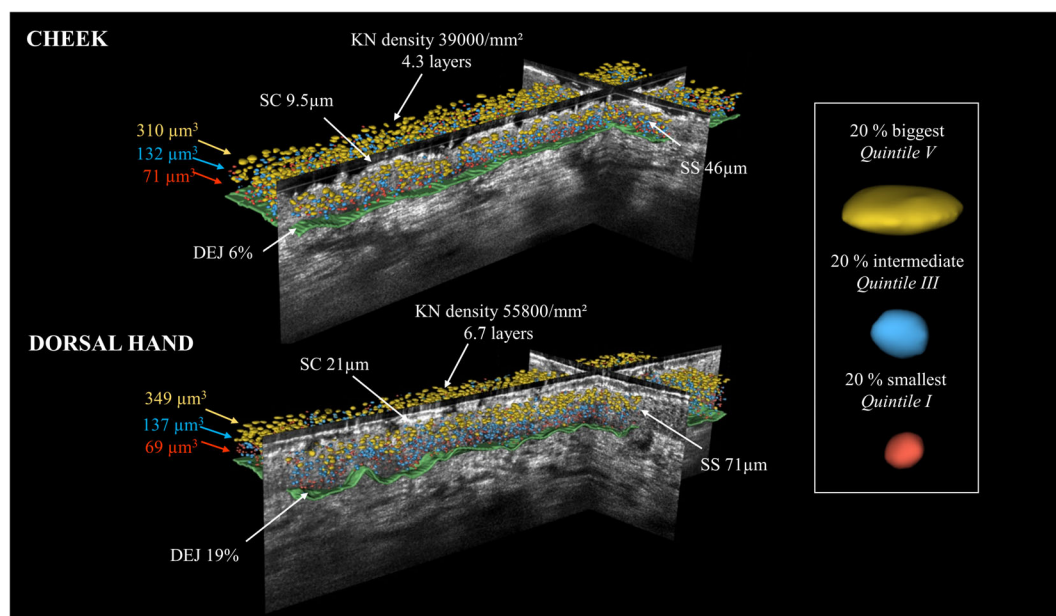
FIGURE 3 Keratinocyte nuclei distribution according to their volume (level of keratinocyte maturation) on the cheek and dorsal hand of the same study participant (21-year-old female, phototype II). Keratinocytes are illustrated in 3D and colored according to nuclei volume (red, quintile I including the smallest; blue, quintile III including the intermediate; yellow, quintile V including the biggest). The dermal-epidermal junction is depicted as a green layer (undulation index expressed in percentage). Three distinct layers are visible: a lower, red layer (just above the DEJ) containing small, immature basal keratinocytes; an intermediate, blue layer containing maturing keratinocytes; and an upper, yellow layer containing large, mature keratinocytes. DEJ, dermal epidermal junction; KN, keratinocytes; SC, stratum corneum; SS, stratum spinosum. Thicknesses (μm); nuclei volume (μm^3); keratinocyte density (mm^{-2})

The level of keratinocyte maturation is illustrated in Figure 3, which shows the keratinocyte nuclei distribution according to their volume across the epidermis.

4 | DISCUSSION

To our knowledge, this is the first study providing an in vivo, quantitative analysis of healthy epidermis using 3D images. The study exploited the recently developed LC-OCT technology, which was previously used in a similar study carried out by Monnier et al. on two-dimensional (2D) images of healthy skin [14]. In line with the results of that preliminary investigation, the present study found that the dorsal hand had the thickest SC as well as the thickest epidermis whereas the cheek had the thinnest SC and the pre-sternal chest the thinnest epidermis. Additionally, the mean thicknesses reported in our study were consistent with those reported by Monnier et al.

Using the 3D LC-OCT technology, we were able to produce unique in vivo images of the DEJ and objectively quantify its undulation. Our findings suggest that the DEJ undulation varies significantly across body sites, the biggest differences being found between the cheek (almost flat) and the back (highly undulated). These data can be useful in dermatology clinical practice to evaluate the DEJ interdigitation index and help dermatologists understand and

quantify features observed in horizontal images obtained with other techniques such as RCM and dermoscopy.

Several limited attempts have quantified DEJ undulation. First, Timar et al. developed the interdigitation index to enable DEJ undulation measurement from histological samples. They found young skin was 20% more undulated than older skin [15]. Although this index was developed for histological samples, it remains valid in vivo which enabled us to extrapolate it to our 3D DEJ undulation calculations. Subsequently, Decencière et al. used multiphoton microscopy to examine the DEJ on the inner forearm skin. They defined the DEJ as a function of the surface area divided by the projection area on a horizontal plane [21]. However, multiphoton microscopy features a smaller field of view ($130 \times 130 \times 164 \ \mu$m^3) and a longer acquisition time (8.5 minutes) than LC-OCT ($1.2 \times 0.5 \times 0.5$ mm^3 in 30 seconds), thus appearing less appropriate for clinical practice and research. Recently, several authors have attempted to quantify DEJ with RCM. Lagarrigue et al. [6] and Kawasaki et al. [22] used a non-automatic quantification method of the dermal papillae density and diameter based on 2D images extracted from a horizontal stack. Kurugol et al. [23], Hames et al. [24] and Robic et al. [25] developed automated algorithms to guide the delineation of the DEJ and Hames et al. [24] proposed a quantification of the DEJ

TABLE 3 Keratinocyte nuclei volume and compactness

Body site	I	II	III	IV	V
Keratinocyte nucleus volume (μm^3)					
Forehead	70 (2)	100 (6)	140 (13)	201 (27)	332 (44)
	69 (2)	98 (6)	137 (12)	195 (24)	322 (44)
	72 (2)	104 (6)	146 (15)	212 (32)	349 (46)
Nose	71 (1)	104 (4)	151 (7)	231 (11)	403 (21)
	71 (1)	102 (2)	148 (4)	227 (11)	397 (24)
	72 (1)	107 (5)	156 (10)	238 (12)	415 (5)
Cheek	74 (3)	110 (9)	154 (17)	216 (27)	354 (42)
	72 (1)	104 (3)	143 (8)	199 (14)	329 (18)
	78 (3)	120 (5)	172 (10)	244 (18)	396 (36)
Chest	73 (3)	106 (9)	149 (19)	196 (20)	327 (23)
	74 (4)	110 (12)	143 (15)	203 (25)	327 (32)
	71 (2)	102 (5)	138 (9)	189 (15)	326 (19)
Back	71 (1)	102 (2)	138 (6)	190 (11)	311 (18)
	71 (1)	101 (3)	136 (7)	186 (12)	305 (17)
	70 (1)	103 (1)	141 (4)	196 (5)	320 (20)
Dorsal forearm	72 (1)	107 (5)	151 (8)	216 (12)	361 (32)
	72 (1)	107 (1)	149 (4)	209 (5)	341 (19)
	72 (3)	107 (9)	153 (14)	227 (11)	392 (14)
Dorsal part of hand	70 (1)	102 (4)	145 (7)	215 (12)	374 (17)
	70 (1)	101 (2)	143 (6)	211 (12)	366 (18)
	71 (2)	103 (6)	149 (9)	223 (8)	387 (5)
Global	72 (3)	104 (7)	146 (12)	210 (22)	353 (40)
	71 (2)	103 (6)	143 (10)	205 (19)	343 (38)
	72 (3)	107 (8)	151 (14)	218 (24)	368 (41)
Keratinocyte nucleus compactness					
Forehead	0.61 (0.02)	0.71 (0.01)	0.76 (0.01)	0.80 (0.01)	0.85 (0.01)
	0.61 (0.02)	0.72 (0.01)	0.77 (0.01)	0.81 (0.01)	0.85 (0.01)
	0.59 (0.03)	0.70 (0.01)	0.75 (0.01)	0.80 (0.01)	0.84 (0.01)
Nose	0.60 (0.02)	0.72 (0.01)	0.77 (0.01)	0.81 (0.01)	0.86 (0.01)
	0.59 (0.02)	0.72 (0.01)	0.77 (0.01)	0.81 (0.01)	0.85 (0.01)
	0.62 (0.01)	0.73 (0.01)	0.78 (0.01)	0.82 (0.01)	0.86 (0.01)
Cheek	0.57 (0.04)	0.69 (0.03)	0.75 (0.02)	0.79 (0.02)	0.85 (0.01)
	0.59 (0.03)	0.71 (0.01)	0.76 (0.01)	0.80 (0.01)	0.85 (0.01)
	0.53 (0.03)	0.66 (0.03)	0.73 (0.02)	0.78 (0.02)	0.84 (0.01)
Chest	0.60 (0.01)	0.70 (0.01)	0.75 (0.01)	0.79 (0.01)	0.84 (0.01)
	0.60 (0.01)	0.70 (0.01)	0.74 (0.01)	0.79 (0.01)	0.84 (0.01)
	0.60 (0.01)	0.71 (0.01)	0.75 (0.01)	0.79 (0.01)	0.84 (0.01)
Back	0.61 (0.01)	0.71 (0.01)	0.76 (0.01)	0.80 (0.01)	0.85 (0.01)
	0.61 (0.01)	0.71 (0.01)	0.76 (0.01)	0.80 (0.01)	0.85 (0.01)
	0.61 (0.02)	0.71 (0.02)	0.76 (0.02)	0.80 (0.02)	0.84 (0.01)
Dorsal forearm	0.61 (0.01)	0.72 (0.01)	0.77 (0.01)	0.81 (0.01)	0.85 (0.01)
	0.62 (0.01)	0.72 (0.01)	0.77 (0.01)	0.81 (0.01)	0.85 (0.01)
	0.60 (0.01)	0.72 (0.01)	0.77 (0.02)	0.81 (0.01)	0.86 (0.01)

TABLE 3 (Continued)

Body site	I	II	III	IV	V
Dorsal part of hand	0.62 (0.01)	0.73 (0.01)	0.78 (0.01)	0.81 (0.01)	0.86 (0.01)
	0.62 (0.02)	0.72 (0.01)	0.77 (0.01)	0.81 (0.01)	0.85 (0.01)
Global	0.61 (0.02)	0.71 (0.02)	0.77 (0.01)	0.81 (0.01)	0.85 (0.01)
	0.60 (0.03)	0.70 (0.03)	0.76 (0.02)	0.80 (0.01)	0.85 (0.01)

Note: Keratinocyte volume and compactness are divided into 5 quintiles according to distribution percentiles (%): I: 0-20%, II: 20-40%, III: 40-60%, IV: 60-80% and V: 80-100%. The compactness score ranges from 0 to 1, where the value for a perfect sphere is 1. For each quintile, the first column shows the overall mean value and the second column shows the mean value for the younger group (top line) and older group (bottom line).

based on a global measurement of its axial extension. Newton et al. [26] suggested a novel approach by which they characterized the DEJ as a function of median plane areas from papillae and rete ridge heights obtained from RCM-derived 3D images. The main limitation of these promising approaches is the limited axial resolution that could impact the accuracy of the measurements.

Furthermore, we were able to quantify keratinocyte nuclei in vivo. We showed an independent measure of epidermal thickness using an automatic recognition technology [17] that characterizes keratinocyte spherical shape, volume and spatial distribution within the epidermis. Indeed, we found the number of nuclei layers directly correlated with epidermal thickness. Concerning spatial repartition, the largest, most elliptical shaped keratinocytes appeared at the top of the epidermis whereas the smallest, roundest cells were closer to the basal layer. This progressive flattening/enlarging of keratinocyte nuclei towards the epidermal surface corresponds with keratinocyte maturation.

Keratinocyte nuclei volumes differed across body sites and age groups, the biggest was on older nasal skin while the smallest was on younger dorsal skin. This suggests that keratinocyte maturation process may vary with age and anatomic location. Conversely, the keratinocyte density did not differ with age. This is in line with a previous histological investigation performed on biopsies from six male adults, which found a very similar keratinocyte density [27].

To our knowledge, no other studies of skin microanatomy with this level of detail and in vivo are available in the literature. Previous research in the field was largely based on histological data, with only few attempts based on RCM. Rajadhyaksha et al. manually measured the size of keratinocytes on horizontal sections at several different depths and found larger cells near the surface than in the basal layer [5]. Shahriari et al. described the keratinocyte layers as a regular honeycomb pattern, but did not characterize individual keratinocyte shape [28]. Gareau et al. developed an algorithm that enabled them to detect nuclei with a 9 μm diameter (and, therefore, to count individual keratinocytes), but not to evaluate volume, shape or maturation level in the epidermis [29]. Previously, Huzaira et al. performed in vivo morphometric analyses of the skin based upon horizontal images but not in 3D [30]. The results of the present study suggest that LC-OCT could be potentially regarded as the tool providing the highest level of quantitative measurement of keratinocytes in vivo.

Combining LC-OCT images with AI algorithms enabled us to measure several epidermal metrics. This may open different clinical and research applications. For instance, LC-OCT may be a valuable tool to describe the effects of skin aging or to investigate the effect of topical treatments. Additionally, LC-OCT might help to recognize disorders in which the keratinocyte maturation is

affected, such as actinic keratosis, or in which other cell types (e.g., inflammatory cells or melanocytes) are involved. Moreover, skin tumor's microenvironment could be characterized by combining LC-OCT with AI, similar to a recent attempt by Kieman et al. who used machine learning algorithms from reconstructed histological sections of pancreatic cancer [31].

Lastly, further development of automatic tools might help non-expert clinicians interpret LC-OCT images and improve diagnostic accuracy for benign (melanocytic proliferations [32], sebaceous hyperplasia [33], circumscribed palmar hypokeratosis [34]) and malignant (BCC [35, 36], Kaposi sarcoma [37], actinic keratosis/squamous cell carcinoma [12, 38–41]) tumors, autoimmune/inflammatory conditions (bullous diseases [42], aquagenic keratoderma [43] lichenoid dermatoses [44]) and infections/infestations (herpes [45], molluscum contagiosum [46], mite [47], *sarcoptes scabiei* [48]).

The main limitation of this pilot investigation was the relatively small sample size. Nevertheless, 56 LC-OCT 3D image blocks (i.e., 28 000 vertical images in total), representing different body areas were analyzed in this study. Also, the ground truth labels used for training the AI algorithm contained some noise, making it very difficult to compute quantitative measurements of model performances. However, a careful, qualitative review of all images and segmentations used in this study was performed by an expert operator to ensure correct segmentations. Future studies are needed to confirm our results, in particular including larger populations, a broader age range to better characterize the age effect on healthy epidermis, and including the quantification of the AI model accuracy. It would also be valuable in further studies to get coupled LC-OCT/histology images of the exact same areas.

5 | CONCLUSION

In conclusion, LC-OCT is an innovative skin imaging technique that produces 3D images at selected locations in vivo and in real time. The automatic quantification of skin features imaged by LC-OCT by means of AI could enable researchers to make reliable analyses of epidermal metrics that can be applied to both basic and clinical research as well as current clinical practice.

AUTHOR CONTRIBUTIONS
Mélanie Pedrazzani, Jean L. Perrot, Mariano Suppa, Elisa Cinotti and Joseph Malvehy contributed to the conception and design of the study. Mélanie Pedrazzani and Randa Jdid were involved in data acquisition and all authors were involved in the data interpretation, critically reviewed the manuscript and approved the version to be published.

DATA AVAILABILITY STATEMENT
The data that support the findings of this study are available from the corresponding author upon reasonable request.

ORCID
Mélanie Pedrazzani https://orcid.org/0000-0003-1399-0181
Elisa Cinotti https://orcid.org/0000-0002-4009-0659
Mariano Suppa https://orcid.org/0000-0002-9266-0342

REFERENCES
[1] S. O'Leary, A. Fotouhi, D. Turk, P. Sriranga, A. Rajabi-Estarabadi, K. Nouri, S. Daveluy, D. Mehregan, M. Nasiriavanaki, *Skin Res. Technol.* **2018**, *24*, 570.
[2] E. Cinotti, C. Bovi, G. Tonini, B. Labeille, C. Heusèle, C. Nizard, S. Schnebert, S. Aubailly, J. C. Barthélémy, F. Cambazard, G. Cevenini, L. Tognetti, A. Cartocci, P. Rubegni, J.-L. Perrot, *J. Eur. Acad. Dermatol. Venereol.* **2020**, *34*, 2652.
[3] C. Longo, A. Casari, F. Beretti, A. M. Cesinaro, G. Pellacani, *J. Am. Acad. Dermatol.* **2013**, *68*, e73.
[4] C. Longo, *Dermatol. Clin.* **2016**, *34*, 513.
[5] M. Rajadhyaksha, S. González, J. M. Zavislan, R. Rox Anderson, R. H. Webb, *J. Invest. Dermatol.* **1999**, *113*, 293.
[6] S. G. Lagarrigue, J. George, E. Questel, C. Lauze, N. Meyer, J.-M. Lagarde, M. Simon, A.-M. Schmitt, G. Serre, C. Paul, *Exp. Dermatol.* **2012**, *21*, 281.
[7] A. Dubois, O. Levecq, H. Azimani, A. Davis, J. Ogien, D. Siret, A. Barut, *Opt. Express* **2018**, *26*, 33534.
[8] A. Dubois, O. Levecq, H. Azimani, D. Siret, A. Barut, M. Suppa, V. Del Marmol, J. Malvehy, E. Cinotti, P. Rubegni, J.-L. Perrot, *J. Biomed. Opt.* **2018**, *23*, 1.
[9] J. Ogien, O. Levecq, H. Azimani, A. Dubois, *Biomed. Opt. Express* **2020**, *11*, 1327.
[10] J. Ogien, A. Daures, M. Cazalas, J.-L. Perrot, A. Dubois, *Front. Optoelectron.* **2020**, *13*, 381.
[11] F. Farnetani, A. Scope, L. Mazzoni, V. D. Mandel, M. Manfredini, S. Magi, C. Vaschieri, S. Kaleci, C. Longo, S.

Ciardo, I. Stanganelli, G. Pellacani, *J. Eur. Acad. Dermatol. Venereol.* **2019**, *33*, 2273.

[12] C. Ruini, S. Schuh, C. Gust, D. Hartmann, L. E. French, E. C. Sattler, J. Welzel, *Cancer* **2021**, *13*, 2856.

[13] M. Pedrazzani, J. Breugnot, P. Rouaud-Tinguely, M. Cazalas, A. Davis, S. Bordes, A. Dubois, B. Closs, *Skin Res. Technol.* **2020**, *26*, 398.

[14] J. Monnier, L. Tognetti, M. Miyamoto, M. Suppa, E. Cinotti, M. Fontaine, J. Perez, C. Orte Cano, O. Yélamos, S. Puig, A. Dubois, P. Rubegni, V. Marmol, J. Malvehy, J.-L. Perrot, *J. Eur. Acad. Dermatol. Venereol.* **2020**, *34*, 2914.

[15] F. Timar, G. Soos, B. Szende, A. Horvath, *Skin Res. Technol.* **2000**, *6*, 17.

[16] C. Shorten, T. M. Khoshgoftaar, *J. Big Data* **2019**, *6*, 60.

[17] M. Weigert, U. Schmidt, R. Haase, K. Sugawara, G. Myers, in *2020 IEEE Winter Conference on Applications of Computer Vision*, Snowmass Village, USA, March **2020**; p. 3655.

[18] H. Wadell, *J. Geol.* **1932**, *40*, 443.

[19] E. J. Limkin, S. Reuzé, A. Carré, R. Sun, A. Schernberg, A. Alexis, E. Deutsch, C. Ferté, C. Robert, *Sci. Rep.* **2019**, *9*, 4329.

[20] H. Park, S. Lee, M. Ji, K. Kim, Y. Son, S. Jang, Y. Park, *Sci. Rep.* **2016**, *6*, 34257.

[21] E. Decencière, E. Tancrède-Bohin, P. Dokládal, S. Koudoro, A.-M. Pena, T. Baldeweck, *Skin Res. Technol.* **2013**, *19*, 115.

[22] K. Kawasaki, K. Yamanishi, H. Yamada, *Int. J. Dermatol.* **2015**, *54*, 295.

[23] S. Kurugol, K. Kose, B. Park, J. G. Dy, D. H. Brooks, M. Rajadhyaksha, *J. Invest. Dermatol.* **2015**, *135*, 710.

[24] S. C. Hames, M. Ardigo, H. P. Soyer, A. P. Bradley, T. W. Prow, in *2015 International Conference on Digital Image Computing: Techniques and Applications (DICTA)*, Australia, November **2015**; p. 1.

[25] J. Robic, B. Perret, A. Nkengne, M. Couprie, H. Talbot, *J. Med. Imaging* **2019**, *6*, 024003.

[26] V. L. Newton, R. S. Bradley, P. Seroul, M. Cherel, C. E. M. Griffiths, A. V. Rawlings, R. Voegeli, R. E. B. Watson, M. J. Sherratt, *Skin Res. Technol.* **2017**, *23*, 131.

[27] P. R. Bergstresser, R. J. Pariser, J. R. Taylor, *J. Invest. Dermatol.* **1978**, *70*, 280.

[28] N. Shahriari, J. M. Grant-Kels, H. Rabinovitz, M. Oliviero, A. Scope, *J. Cutan. Pathol.* **2018**, *45*, 187.

[29] D. Gareau, R. Hennessy, E. Wan, G. Pellacani, S. L. Jacques, *J. Biomed. Opt.* **2010**, *15*, 061713.

[30] M. Huzaira, F. Rius, M. Rajadhyaksha, R. R. Anderson, S. González, *J. Invest. Dermatol.* **2001**, *116*, 846.

[31] A. Kiemen, A. M. Braxton, M. P. Grahn, K. S. Han, J. M. Babu, R. Reichel, F. Amoa, S.-M. Hong, T. C. Cornish, E. D. Thompson, L. D. Wood, R. H. Hruban, P.-H. Wu, D. Wirtz, *bioRxiv* **2020**, 2020.12.08.416909.

[32] C. Lenoir, J. Perez-Anker, G. Diet, L. Tognetti, E. Cinotti, A. L. Trépant, P. Rubegni, S. Puig, J. L. Perrot, J. Malvehy, V. Del Marmol, M. Suppa, *J. Eur. Acad. Dermatol. Venereol.* **2021**, *35*, e399.

[33] C. Lenoir, G. Diet, E. Cinotti, L. Tognetti, C. Orte Cano, L. Rocq, A.-L. Trépant, J. Monnier, J. Perez-Anker, P. Rubegni, S. Puig, J. Malvehy, J.-L. Perrot, V. Del Marmol, M. Suppa, *J. Eur. Acad. Dermatol. Venereol.* **2021**, *35*, e509.

[34] L. Tognetti, D. Fiorani, M. Suppa, E. Cinotti, M. Fontaine, V. Del Marmol, P. Rubegni, J. L. Perrot, *Indian J. Dermatol. Venereol. Leprol.* **2020**, *86*, 206.

[35] M. Suppa, M. Fontaine, G. Dejonckheere, E. Cinotti, O. Yélamos, G. Diet, L. Tognetti, M. Miyamoto, C. Orte Cano, J. Perez-Anker, V. Panagiotou, A. L. Trepant, J. Monnier, V. Berot, S. Puig, P. Rubegni, J. Malvehy, J. L. Perrot, V. Del Marmol, *J. Eur. Acad. Dermatol. Venereol.* **2021**, *35*, 1099.

[36] C. Ruini, S. Schuh, C. Gust, B. Kendziora, L. Frommherz, L. E. French, D. Hartmann, J. Welzel, E. Sattler, *Clin. Exp. Dermatol.* **2021**.

[37] L. Tognetti, A. Carraro, A. Lamberti, E. Cinotti, M. Suppa, J. L. Perrot, P. Rubegni, *Skin Res. Technol.* **2021**, *27*, 285.

[38] G. Dejonckheere, M. Suppa, V. Del Marmol, T. Meyer, E. Stockfleth, *J. Eur. Acad. Dermatol. Venereol.* **2019**, *33*, 16.

[39] E. Cinotti, L. Tognetti, A. Cartocci, A. Lamberti, S. Gherbassi, C. Orte Cano, C. Lenoir, G. Dejonckheere, G. Diet, M. Fontaine, M. Miyamoto, J. Perez-Anker, V. Solmi, J. Malvehy, V. del Marmol, J. L. Perrot, P. Rubegni, M. Suppa, *Clin. Exp. Dermatol.* **2021**.

[40] C. Ruini, S. Schuh, C. Gust, B. Kendziora, L. Frommherz, L. E. French, D. Hartmann, J. Welzel, E. C. Sattler, *J. Eur. Acad. Dermatol. Venereol.* **2021**.

[41] C. Lenoir, E. Cinotti, L. Tognetti, C. Orte Cano, G. Diet, M. Miyamoto, L. Rocq, A.-L. Trépant, J. Perez-Anker, S. Puig, J. Malvehy, P. Rubegni, J.-L. Perrot, V. Marmol, M. Suppa, *J. Eur. Acad. Dermatol. Venereol.* **2021**.

[42] L. Tognetti, E. Cinotti, M. Suppa, R. Guazzo, C. Habougit, F. Santi, G. Diet, M. Fontaine, V. Berot, J. Monnier, E. Pianigiani, V. Del Marmol, J. Malvehy, J. L. Perrot, P. Rubegni, *J. Biophotonics* **2021**, *14*, e202000449.

[43] L. Tognetti, D. Fiorani, E. Cinotti, P. Rubegni, *Int. J. Dermatol.* **2020**, *60*, e52.

[44] L. Tognetti, A. Carraro, E. Cinotti, M. Suppa, V. Marmol, J. L. Perrot, P. Rubegni, *Skin Res. Technol.* **2021**.

[45] F. Lacarrubba, A. E. Verzì, D. F. Puglisi, G. Micali, *J. Eur. Acad. Dermatol. Venereol.* **2021**, *35*, e404.

[46] A. E. Verzì, G. Micali, F. Lacarrubba, *J. Eur. Acad. Dermatol. Venereol.* **2021**.

[47] C. Ruini, S. Schuh, D. Hartmann, L. French, J. Welzel, E. Sattler, *Br. J. Dermatol.* **2021**, *184*, e3.

[48] C. Ruini, S. Schuh, G. Pellacani, L. French, J. Welzel, E. Sattler, *J. Eur. Acad. Dermatol. Venereol.* **2020**, *34*, e808.